Bubble nucleation and migration in a lead–iron hydr(oxide) core–shell nanoparticle

Kaiyang Niu[a], Timofey Frolov[b], Huolin L. Xin[a], Junling Wang[c], Mark Asta[b], and Haimei Zheng[a,b,1]

[a]Materials Sciences Division, Lawrence Berkeley National Laboratory, Berkeley, CA 94720; [b]Department of Materials Science and Engineering, University of California, Berkeley, CA 94720; and [c]School of Materials Science and Engineering, Nanyang Technological University, Singapore 639798

Edited by Alexis T. Bell, University of California, Berkeley, CA, and approved September 10, 2015 (received for review May 26, 2015)

Iron hydroxide is found in a wide range of contexts ranging from biominerals to steel corrosion, and it can transform to anhydrous oxide via releasing O_2 gas and H_2O. However, it is not well understood how gases transport through a crystal lattice. Here, we present in situ observation of the nucleation and migration of gas bubbles in iron (hydr)oxide using transmission electron microscopy. We create Pb–FeOOH model core–shell nanoparticles in a liquid cell. Under electron irradiation, iron hydroxide transforms to iron oxide, during which bubbles are generated, and they migrate through the shell to the nanoparticle surface. Geometric phase analysis of the shell lattice shows an inhomogeneous stain field at the bubbles. Our modeling suggests that the elastic interaction between the core and the bubble provides a driving force for bubble migration.

bubbles | nucleation | liquid cell | TEM | core–shell nanoparticle

Gas bubble formation in a solid is commonly observed and its migration dynamics is of both scientific and engineering importance (1, 2). For instance, in recent years there has been increasing interest in solution processing of materials for energy conversion and storage applications (3). Dehydration of as-synthesized materials to form anhydrous phases is a critical step (4), where gaseous species are often generated during the reaction. As a consequence, materials may become porous or deformed, and properties can be altered accordingly. Gas bubble formation is key to many other materials processes as well, including embrittlement and cracking in the nuclear reactor cladding due to neutron radiation (5), food preservation (6), seismic events in the earth's mantle (7), etc. Gas bubbles in a liquid can be released easily to the surface through a pressure gradient (8). However, high temperature annealing is often needed (i.e., up to 1,400 °C) to remove bubbles from a solid (9), because it involves a large number of atoms' correlated movements. To understand how bubbles propagate and migrate through a crystal lattice, it is necessary to monitor the processes in situ and quantify the structural evolution dynamics. So far, however, there have been limited real-time studies on the bubbles propagation in solid materials, especially while the materials are under chemical reactions in a liquid environment.

Here, we made Pb–FeOOH core–shell nanoparticles in a liquid cell under transmission electron microscopy (TEM) (10–12). The iron hydroxide shell undergoes dehydration reaction upon electron irradiation and release gaseous species. Because different phases of gas, solid, and liquid are involved in such a dehydration reaction, it is a challenge to visualize the bubble evolution with high spatial resolution and to map dynamic strain distribution within the crystal lattice. In this work, we have been able to monitor the evolution of gas bubbles during the dehydration process using homemade liquid cells under TEM. By tracking the dynamic strain distribution in the core–shell nanoparticle, we have obtained an unprecedented level of details on the evolution and migration of nanobubbles in the nanoparticle while the chemical reactions are proceeding in a wet environment. Geometric phase analysis (GPA) of the shell lattice reveals an inhomogeneous stain field at the bubbles. Our computational modeling suggests that the elastic interaction between the core and the bubble provides a driving force for bubble migration.

Results and Discussion

Bubble Nucleation and Growth. We synthesized Pb–FeOOH (β) core–shell nanoparticles inside a liquid cell as the model system. A precursor solution of Pb(acetylacetonate)$_2$ and Fe(acetylacetonate)$_2$ (molar ratio of Pb:Fe is 1:2) dissolved in triethylene glycol was used. The growth of nanoparticles was achieved by the electron beam irradiation at lower magnification under TEM with a beam current density of ~500 electrons·Å^{-2}·s^{-1}. The Pb–FeOOH (β) core–shell nanoparticles were obtained through the phase separation of lead and iron species (note that Pb and Fe are immiscible on Pb–Fe phase diagram). An TEM image of the core–shell nanoparticle is shown in Fig. 1*A*, where the 10-nm Pb core is off-centered in the 30-nm iron hydroxide matrix. The structural identification of the as-synthesized nanoparticle using high-resolution TEM images is shown in Fig. S1 and Table S1. Under continuous electron beam irradiation with a beam current density of ~1,000 electrons · Å^{-2} · s^{-1}, the iron hydroxide is not stable and transforms into iron oxide (13, 14), where gas bubbles containing H_2O, O_2, and H_2 are generated from the dehydration of the hydroxide and the radiolysis of water under the electron beam (*Supporting Information*).

A large number of bubbles are observed in the nanoparticle at the core–shell interface (Fig. 1*B* and Fig. S2; Movies S1 and S2). It is expected that the gaseous reaction products, including O_2 and H_2O, could accumulate at the core–shell interface or inside the iron (hydr)oxide lattice, which is intrinsically a highly defective material (15). The as-generated H_2O molecules can further undergo radiolysis to produce radicals (e_{aq}^-, H·, and ·OH) and molecular products (H_2 and H_2O_2) under electron beam

Significance

An understanding of gas bubble formation in a solid and the materials' responses at the nanoscale is of technological importance. Tracking nanobubble evolution in a solid during chemical reactions involving a solid, a gas, and a liquid is rarely achieved. Here, we show a breakthrough in materials characterization by monitoring gas bubble nucleation and migration and the associated strain evolution in a lead–iron hydroxide core–shell nanoparticle during dehydration reaction using liquid cell transmission electron microscopy. We found strain coupling can be used to remove gas bubbles from nanostructures, which sheds light on strategies for nanomaterials engineering and novel materials synthetic routes.

Author contributions: K.N. and H.Z. designed research; K.N. performed research; K.N., T.F., H.L.X., J.W., M.A., and H.Z. analyzed data; T.F., H.L.X., and M.A. contributed new reagents/analytic tools; and K.N., J.W., M.A., and H.Z. wrote the paper.

The authors declare no conflict of interest.

This article is a PNAS Direct Submission.

[1]To whom correspondence should be addressed. Email: hmzheng@lbl.gov.

This article contains supporting information online at www.pnas.org/lookup/suppl/doi:10.1073/pnas.1510342112/-/DCSupplemental.

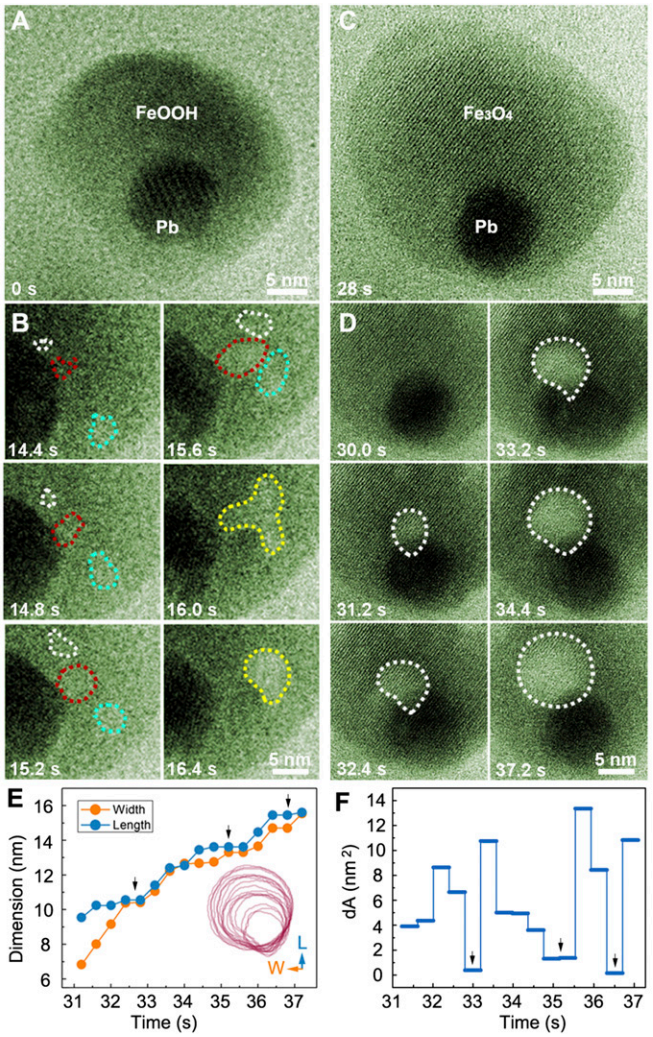

Fig. 1. Nucleation and growth dynamics of bubbles in lead–iron (hydr)oxide core–shell nanocrystal. (*A*) TEM image of the Pb–FeOOH(β) core–shell nanoparticle formed in a liquid cell. (*B*) Sequential images showing three growing bubbles at the core–shell interface and coalesce into one bubble later. (*C*) TEM image of the Pb–iron oxide core–shell nanoparticle resulted from the phase transition of the initial Pb–FeOOH(β) core–shell nanoparticle under the electron irradiation. (*D*) Sequential images showing a growing bubble at the core–shell interface. (*E*) Evolution of the growing nanobubble in *D* and the *Inset* is the trajectory of contours of the bubble. (*F*) Change in area of the projected shape of the growing bubble with time.

irradiation (16, 17). Therefore, the propagating nanobubbles should be filled with gaseous molecules of O_2, H_2O, or H_2. Most bubbles nucleate at the core–shell interface, which has lower energy barrier for the bubble nucleation and growth (18, 19). The bubbles grow and migrate rapidly through the shell, and coalescence of bubbles is also observed (Movie S3). The elastic interaction between the core and the shell may provide a driving force for bubble migration. The role of core–shell interface in bubble migration including the elastic energy estimation has been provided in the later section of this paper.

Fig. 1 *C* and *D* illustrates the process where a bubble nucleates at the core–shell interface and grows to 13 nm in diameter. Meanwhile, a deformation of the shell is observed, where a phase transition from iron hydroxide to iron oxide (likely Fe_3O_4; see detailed analysis in *Supporting Information*) occurs. The shell is flattened (thinner in the vertical direction) from the drastic atom rearrangement of the crystal lattice during the phase transformation and bubble propagation, as shown by the lighter contrast of the particle in its sequential images. Detailed analysis of the bubble formation at interfaces shows that the bubble changes its shape dynamically while it is pinned at the interface. The bubble growth trajectories show stepwise propagation characteristics (Fig. 1 *E* and *F*). It is clear that bubble enlargement involves the movement of a large number of atoms and the accumulation of vacancies and gas molecules. When the edge of the bubble reaches the nanoparticle surface, it disappears rapidly.

Strain Analysis. We map the local strain distribution within the nanoparticle using GPA on the sequential high-resolution TEM images acquired from the in situ experiments. A circular mask with certain radius is chosen in reciprocal space, such that its boundary is tangential to a Brillouin zone boundary, to maximize the resolution of GPA (20). We take the reference with the reciprocal lattice g vectors that best optimize the signal-to-noise ratio to calculate the geometric phase images $P_g(r)$. Any displacement of the lattice fringes with respect to the selected reference will result in a phase shift, i.e., a change in the value of the phase at the position corresponding to the displacement. The geometric phase obtained here is related to one-dimensional lattice displacement field $u_x(r)$ along the x direction, where $u_x(r) = -(1/2\pi) \cdot P_g(r) \cdot g$, and the g vector (111) is used for the displacement field determination in iron oxide. The x direction is normal to (111) plane of iron oxide (Fe_3O_4). The local distortion of the lattice around the core–shell interface, ε, is given by the gradient of the displacement field ($\varepsilon_x = \delta u_x(r)/\delta x$), which indicates the corresponding strain field, ε_x, along the x direction. In Fig. 2, the GPA maps show that the shell lattice around the bubble has a tensile strain up to 1.5% ± 0.3% (discussions on the measurement error is provided in *Supporting Information*, and Figs. S3–S5). The tensile strain is observed before the bubble is visible, which suggests that H_2O and O_2 molecules accumulate in the local area (Fig. 2 and Fig. S3). The shell lattice around the core shows a compressive strain of about 1.0% ± 0.3%. During bubble growth, strain distribution around the bubble and the core changes, where the shell lattice maintains a positive strain around the bubble and a negative strain around the core (Movie S4). The same trend has been observed in other bubbles and the tensile stain likely results from the gas pressure inside the bubble (*Supporting Information*).

Bubble Migration Dynamics. The sequential high resolution TEM images in Fig. 3 show the shape evolution of two bubbles migrating through the shell, during which the shell experiences phase transition and shape deformation. In both cases, the shell maintains a single crystal lattice during bubble migration. As shown in Fig. 3 *A* and *B*, the surface configuration of the bubble changes with periodic enhancements in the isotropy of the shapes as bubble migrates inside the shell lattice. Here, isotropy (0~1.0) is measured by the ratio of the perimeter of the bubble to that of a circular object with the same size, with a value of 1.0 corresponding to a circular projected shape. Because the bubble can absorb nearby vacancies (or small bubble precipitates) during migration (21), possible concentration fluctuations of vacancies (bubble precipitates) in the bubble peripheral area may contribute to the shape changes. On the other hand, the accompanying strain close to the bubble could also facilitate the shape changes, as well as the deformation of the particle. The approximately circular average projected shape suggests that surface energy is approximately isotropic. When a bubble moves out of the lattice (Fig. 3 *C*–*E*), curvature of the bubble is gradually reduced until a perfect crystal lattice is restored. The high structural flexibility of nanoparticles has been observed in other liquid processing of materials (22). The process of bubble nucleation and migration out of the particle represents an effective mechanism for transport of gas species in a solid.

We measure the speed of bubble migration and its dependence on bubble sizes (Fig. 4). Trajectories of five bubbles

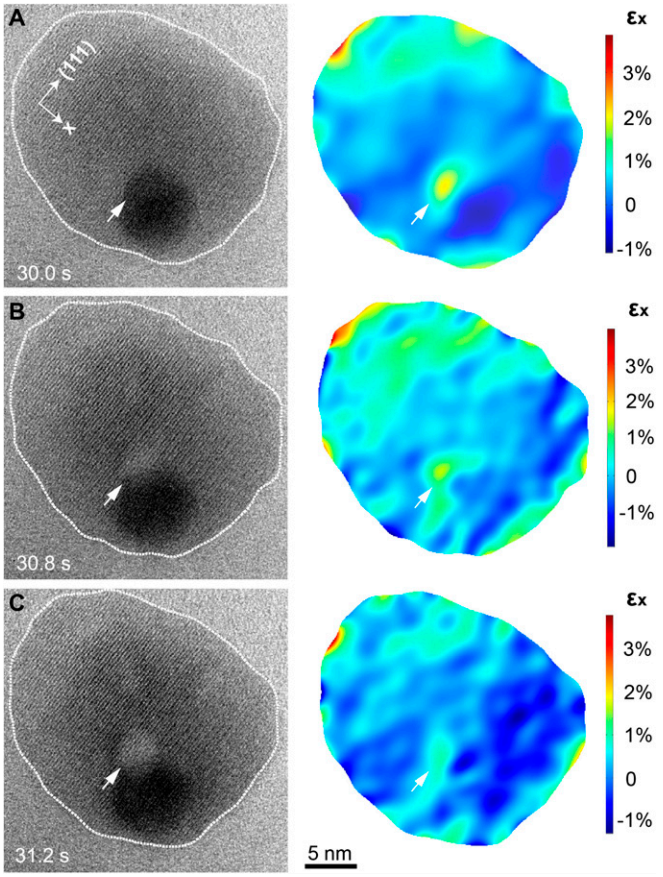

Fig. 2. Strain distribution maps of the core–shell nanoparticle during nucleation and growth of a bubble at the interface. (*A*–*C*) TEM image series and the corresponding strain field (ε_x) calculated from the (111) Bragg reflection of the iron oxide (Fe_3O_4) shell during the bubble propagation. The white lines in the TEM images define the selected shell lattice for GPA; the arrows mark the same positions in the particle as references.

with the diameters of 3.1, 4.0, 4.8, 5.4, and 5.8 nm (marked as 1, 2, 3, 4, and 5, respectively) show that all of the bubbles migrate directly from the core–shell interface to the particle surface. Each bubble has a near constant speed of migration and an average velocity of 2.56, 2.81, 1.90, 1.74, and 1.46 nm/s are observed. The larger bubbles moves slightly slower than the smaller ones, however, the size effect on bubble migration is not significant. The speed of migration increases when a bubble moves near the crystal surface before it vanishes (captured for bubbles 4 and 5).

It is noted that the observed bubble migration in this work is different from those solely under high-temperature heating (23, 24), where Brownian motion occurs. In the present work, bubbles migrate with a nearly constant speed along one direction toward the surface. Based on the analysis of bubble evolution after coalescence, we propose that bubble migration is primarily mediated by the surface diffusion (Fig. S6; *Supporting Information*). The bubble migration observed here is also different from other reported irradiation-induced bubbles (or voids) by high-energy particles under high temperatures, such as neutrons, α-particles, and electrons (Tables S2 and S3), where bubbles (or voids) mostly stay inside the solid (25–27). It has been reported that the temperature rise in a liquid cell induced from the electron beam irradiation is small (only a few degrees or less) (28–30), therefore, we consider a critical factor, i.e., the elastic strain contribution to the observed bubble migration rather than the electron beam heating.

The Role of Elastic Energy in Bubble Migration. We use molecular statics calculations to investigate the nature of the elastic interaction between the core particle and bubbles. To explore the generic behavior, we created a core–shell particle with interactions between atoms described by a simple model interatomic potential for a metal. Uniform 1% compressive and tensile strain was applied to two cylindrical regions inside the particle to mimic the core and the bubble, respectively. Details of the modeling are available in *Methods* and *Supporting Information*. The long-range elastic strain generated by the core and the bubble is illustrated in Fig. 5*A*. The calculated elastic energy as a function of the core–bubble distance is plotted in Fig. 5*B* for the bubbles with different sizes. The elastic energy decreases with the core–bubble distance. Therefore, it is energetically favorable for the bubble to move out from the lattice. Without the core, the bubble located far away from the surface would not experience the driving force and would stay in the middle of the particle. Fig. S7 shows the evolution of the gradient of the elastic energy as the core–bubble distance increases. The elastic interaction energy decreases more rapidly as the bubble approaches the surface. Therefore, a bubble should accelerate near the surface as observed in the TEM experiment. The simulated results are in qualitative agreement with our in situ experimental observations.

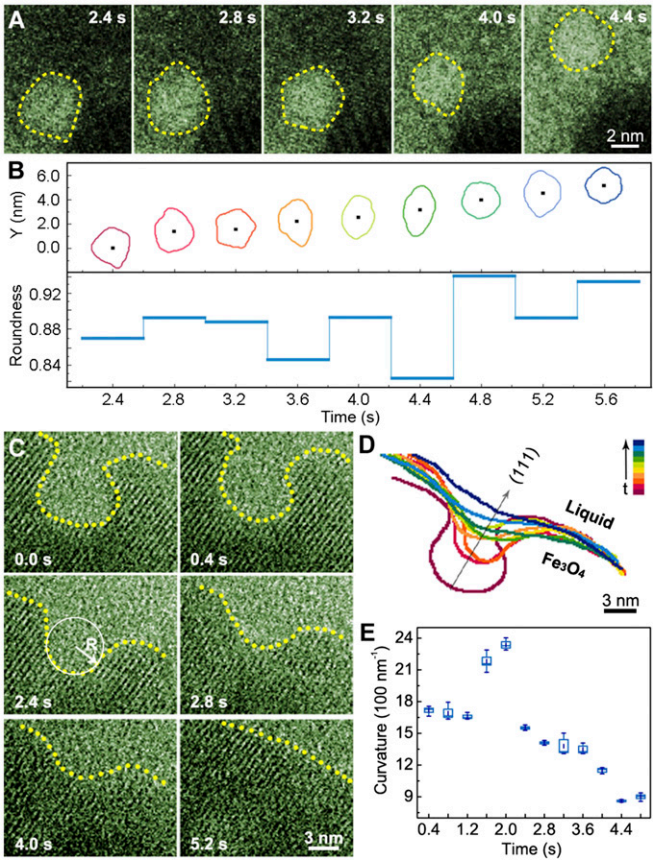

Fig. 3. Shape evolution of two bubbles during migration through the nanocrystal lattice. (*A*) Snapshot TEM images of a migrating bubble in FeOOH with average size of about 4.8 nm. The starting time is arbitrary. (*B*) Migration trajectory and shape changes of the bubble displayed in *A* and the roundness defines the shape factor of the bubble. (*C*) Snapshot TEM image series of a bubble migrating out of the iron oxide shell from Movie S3. *R* is the radius of the bubble, and the starting time is arbitrary. (*D*) Trajectory of the migrating bubble in *C*. (*E*) Curvature evolution of the bubble corresponding to *D*.

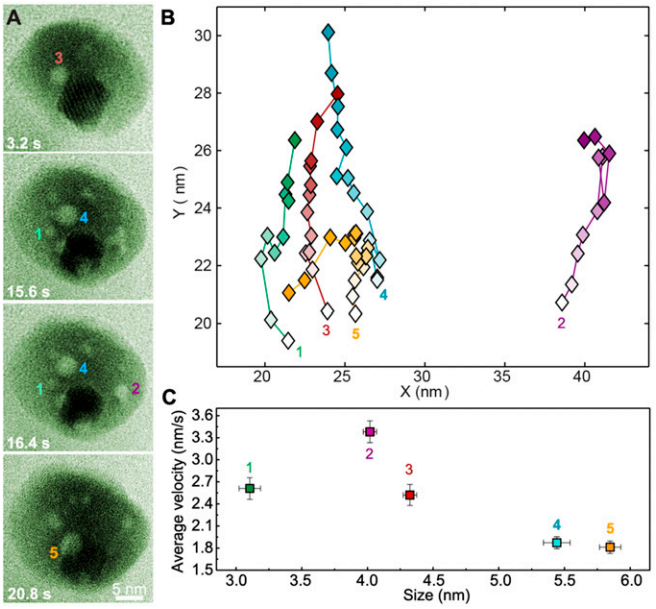

Fig. 4. Migration dynamics of five bubbles. (A) Snapshot TEM images of the bubble migration events. (*B*) Migration trajectories of five bubbles with different sizes. (*C*) Average velocity of different bubbles.

Conclusions

In conclusion, we have observed directly the bubble nucleation and migration in a lead–iron (hydr)oxide core–shell nanoparticle during dehydration reaction induced transformation from iron hydroxide to iron oxide. In situ high-resolution TEM imaging and the dynamic strain analysis allow us to map the strain distribution inside the nanoparticle as it undergoes chemical reactions involving solid, liquid, and gas phases. It is remarkable that bubbles can be pumped out of the solid, during which the single crystal lattice is maintained. Computational modeling illustrates that elastic strain interaction can drive a bubble to move out of the nanoparticle. These findings shed light on strategies of using strain to design defect-free anhydrous materials. The dynamics of bubble nucleation and migration in a crystal lattice may share some similarities with that of the bubbles generated in liquids (8, 17) or in biological systems (31). For instance, precipitation and growth of bubbles induced by gas diffusion and supersaturation have been found in those systems.

Methods

Pb-FeOOH (β) Core–Shell Nanoparticle Synthesis, Bubble Formation, and Movie Acquisition. All chemicals including $Pb(acetylacetonate)_2$ (99%, Aldrich), $Fe(acetylacetonate)_2$ (99%, Aldrich), Triethylene Glycol (99%, Aldrich) are used as received. The Pb–FeOOH (β) core–shell nanoparticles were synthesized by electron beam initiation inside a liquid cell under an TEM in situ. The precursor solution was prepared by dissolving $Pb(acetylacetonate)_2$ and $Fe(acetylacetonate)_2$ (Pb:Fe molar ratio of 1:2) in triethylene glycol at 60 °C. When the electron beam (200 kV; beam current density of about 500 electrons $\cdot$ Å^{-2} $\cdot$ s^{-1}) passes through the silicon nitride window (3 × 50 μm) irradiating the solution, growth of nanoparticles in the liquid was initiated at low magnification under TEM. The bubble formation in a core–shell nanoparticle was initiated under an electron current density of 1,000 electrons $\cdot$ Å^{-2} $\cdot$ s^{-1}. The study of the kinetics of reaction and phase transition was under the same electron beam current density. It is noted that a stronger electron beam current (above 1,500 electrons $\cdot$ Å^{-2} $\cdot$ s^{-1}) introduces undesirable deformation and damage of the core–shell nanoparticle. The movie was recorded at a rate of five frames per second by the open-sourced software VirtualDub embedded in the DigitalMicrograph software. The as-recorded movie was compressed to reduce the file size (480 × 480 pixels), and the movie plays 4 times faster than the original movie. However, all image analysis was done on the original images extracted from the as recorded movie. All movies were acquired using a JEOL 2100 transmission electron microscope with a high-resolution pole piece and a LaB_6 filament. A Gatan Orius CCD camera was used for in situ imaging.

Image Analysis. We used ImageJ software to track the movements of each bubble. The image coloring was performed using the Photoshop software. All original images are available in *Supporting Information*. Further image processing such as image contrast analysis was done using Gatan Digital Micrograph. The stain analysis was conducted using geometric phase analysis.

Molecular Statics Calculations of Core–Bubble Interaction Through Elastic Field. Interaction between bubble and particle is investigated using molecular static simulations. We used Cu as a model material with atomic interactions described by embedded atom method (EAM) potential (32). It is noted that the details of interaction will not be accurate due to choice of model Cu system instead of real lead–iron oxide core–shell structure. However, the calculations can address a general question whether there is a driving force for bubble migration due to elastic interactions. First, we created a perfect crystal with [100] type crystallographic directions parallel to the *x*, *y*, and *z* directions of the simulation block. The dimensions of the block were 40.0 × 40.0 × 0.3615 nm^3. Then a cylindrical region of 20.0-nm radius was cut out from the original crystal. To mimic the core particle, we uniformly scaled the *x* and *y* positions of the atoms inside the cylindrical region with radius 5 nm by 1%. Similarly, we modeled the bubble by applying 1% tensile strain to another cylindrical region located at different distances away from the core. After this core–shell structure with bubble was created the structure was statically relaxed to minimize the total energy using conjugate gradient method implemented in Large-scale

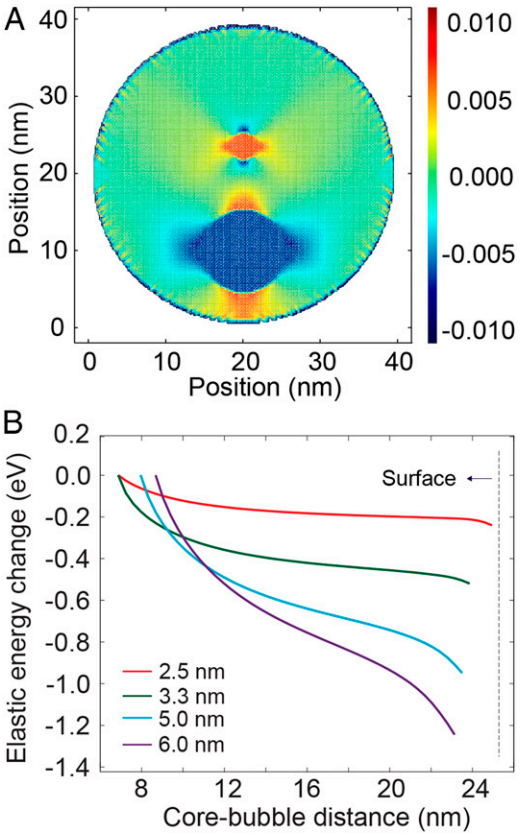

Fig. 5. Core–bubble interaction through an elastic field calculated using molecular statics. (*A*) Atomistic calculations of the migration of a bubble in a lattice with 1% compressive strain applied at the core (dark blue area) and 1% tensile strain applied to the bubble. The elastic interaction between the core and the bubble provides a driving force for the bubble to be expelled from the shell lattice. The colors correspond to strain, which is the component parallel to the line connecting the core and the bubble. It is calculated as the difference between the local lattice spacing between 100 planes and stress-free lattice parameter, divided by stress-free lattice parameter. (*B*) The change in the elastic energy with bubble migration is plotted for bubbles with a diameter of 2.5, 3.3, 5.0, and 6.0 nm; the dashed line shows the approximate surface of the shell.

Atomic/Molecular Massively Parallel Simulator (LAMMPS) (33). During the minimization, the positions of atoms belonging to the core particle remain fixed, and the atoms belonging to the bubble moved as a rigid body. To visualize the elastic field in the particle after the relaxation we colored the atoms according to local strain $e_{xx} = (a_{xx}-a_0)/a_0$, where a_{xx} is the local lattice parameter in the x direction and a_0 is the stress-free parameter of perfect lattice. The x direction is parallel to the line connecting the centers of the core particle and the bubble.

ACKNOWLEDGMENTS. We acknowledge the facility support of National Center for Electron Microscopy of the Molecular Foundry at Lawrence Berkeley National Laboratory, which is funded by US Department of Energy (DOE) Basic Energy Sciences with Contract DE-AC02-05CH11231. T.F. was supported by a Miller Fellowship of University of California (UC), Berkeley. J.W. acknowledges the funding support of National Research Foundation of Singapore under Project NRF-CRP5-2009-04. H.Z. acknowledges the travel support of SinBeRise BEARS UC Berkeley. H.Z. thanks the support of DOE Office of Science Early Career Research Program.

1. Zhang Y, Millett PC, Tonks M, Zhang L, Biner B (2012) Molecular dynamics simulations of He bubble nucleation at grain boundaries. *J Phys Condens Matter* 24(30):305005.
2. Semenov AA, Woo CH (2011) Interfacial energy in phase-field emulation of void nucleation and growth. *J Nucl Mater* 411(1-3):144–149.
3. Jung H-G, Jang MW, Hassoun J, Sun Y-K, Scrosati B (2011) A high-rate long-life $Li_4Ti_5O_{12}$/$Li[Ni_{0.45}Co_{0.1}Mn_{1.45}]O_4$ lithium-ion battery. *Nat Commun* 2:516.
4. Suntivich J, May KJ, Gasteiger HA, Goodenough JB, Shao-Horn Y (2011) A perovskite oxide optimized for oxygen evolution catalysis from molecular orbital principles. *Science* 334(6061):1383–1385.
5. Stan M (2009) Discovery and design of nuclear fuels. *Mater Today* 12(11):20–28.
6. Parthasarathi S, Anandharamakrishnan C (2014) Modeling of shrinkage, rehydration and textural changes for food structural analysis: A review. *J Food Process Eng* 37(2): 199–210.
7. Schmandt B, Jacobsen SD, Becker TW, Liu Z, Dueker KG (2014) Earth's interior. Dehydration melting at the top of the lower mantle. *Science* 344(6189):1265–1268.
8. Krishna R, Van Baten J (1999) Simulating the motion of gas bubbles in a liquid. *Nature* 398(6724):208–208.
9. Kong SY, et al. (2014) Effects of thermal annealing on the evolution of He bubbles in zirconia. *Nucl Instrum Methods Phys Res B* 326:214–218.
10. Niu K-Y, Park J, Zheng H, Alivisatos AP (2013) Revealing bismuth oxide hollow nanoparticle formation by the Kirkendall effect. *Nano Lett* 13(11):5715–5719.
11. Sutter E, et al. (2014) In situ liquid-cell electron microscopy of silver-palladium galvanic replacement reactions on silver nanoparticles. *Nat Commun* 5:4946.
12. Liao H-G, et al. (2014) Nanoparticle growth. Facet development during platinum nanocube growth. *Science* 345(6199):916–919.
13. Musić S, Krehula S, Popović S (2004) Thermal decomposition of β-FeOOH. *Mater Lett* 58(3–4):444–448.
14. Wang S, Xin H (1999) The γ-irradiation-induced chemical change from β-FeOOH to Fe_3O_4. *Radiat Phys Chem* 56(5–6):567–572.
15. Saunders SRJ, Monteiro M, Rizzo F (2008) The oxidation behaviour of metals and alloys at high temperatures in atmospheres containing water vapour: A review. *Prog Mater Sci* 53(5):775–837.
16. Pastina B, LaVerne JA (2001) Effect of molecular hydrogen on hydrogen peroxide in water radiolysis. *J Phys Chem A* 105(40):9316–9322.
17. Grogan JM, Schneider NM, Ross FM, Bau HH (2014) Bubble and pattern formation in liquid induced by an electron beam. *Nano Lett* 14(1):359–364.
18. Kooi BJ, De Hosson JTM (2000) Influence of misfit and interfacial binding energy on the shape of the oxide precipitates in metals: Interfaces between Mn_3O_4 precipitates and Pd studied with HRTEM. *Acta Mater* 48(14):3687–3699.
19. Chan DK, Seidman DN, Merkle KL (1995) Chemistry and structure of CdO/Ag222 heterophase interfaces. *Phys Rev Lett* 75(6):1118–1121.
20. Hÿtch MJ, Putaux J-L, Pénisson J-M (2003) Measurement of the displacement field of dislocations to 0.03 A by electron microscopy. *Nature* 423(6937):270–273.
21. Barnes RS, Mazey DJ (1963) The migration and coalescence of inert gas bubbles in metals. *Proc R Soc Lond A Math Phys Sci* 275(1360):47–57.
22. Liao H-G, Cui L, Whitelam S, Zheng H (2012) Real-time imaging of Pt_3Fe nanorod growth in solution. *Science* 336(6084):1011–1014.
23. Baker C (1977) The migration of intragranular fission gas bubbles in irradiated uranium dioxide. *J Nucl Mater* 71(1):117–123.
24. Evans JH, Eldrup M (1975) Vacancy migration and void formation during annealing of electron irradiated molybdenum. *Nature* 254(5502):685–686.
25. Buckett MI, et al. (1989) Electron-irradiation damage in oxides. *Ultramicroscopy* 29(1-4): 217–227.
26. Zhang X, Lu G (2008) Electronic origin of void formation in fcc metals. *Phys Rev B* 77(17):174102.
27. Xu W, et al. (2013) In-situ atomic-scale observation of irradiation-induced void formation. *Nat Commun* 4:2288.
28. Creemer JF, et al. (2010) A MEMS reactor for atomic-scale microscopy of nanomaterials under industrially relevant conditions. *J Microelectromech Syst.* 19(2):254–264.
29. de Jonge N, Ross FM (2011) Electron microscopy of specimens in liquid. *Nat Nanotechnol* 6(11):695–704.
30. Zheng H, Claridge SA, Minor AM, Alivisatos AP, Dahmen U (2009) Nanocrystal diffusion in a liquid thin film observed by in situ transmission electron microscopy. *Nano Lett* 9(6):2460–2465.
31. Graves DJ, Idicula J, Lambertsen CJ, Quinn JA (1973) Bubble formation in physical and biological systems: A manifestation of counterdiffusion in composite media. *Science* 179(4073):582–584.
32. Mishin Y, Mehl M, Papaconstantopoulos D, Voter A, Kress J (2001) Structural stability and lattice defects in copper: Ab initio, tight-binding, and embedded-atom calculations. *Phys Rev B* 63(22):224106.
33. Plimpton S (1995) Fast parallel algorithms for short-range molecular dynamics. *J Comput Phys* 117(1):1–19.
34. Zheng H, et al. (2009) Observation of single colloidal platinum nanocrystal growth trajectories. *Science* 324(5932):1309–1312.
35. Niu KY, Liao HG, Zheng H (2012) Revealing dynamic processes of materials in liquids using liquid cell transmission electron microscopy. *J Vis Exp* 70(70):e50122.
36. Hÿtch M (1997) Geometric phase analysis of high resolution electron microscope images. *Scanning Microsc* 11:53–66.
37. Aguirre M, Shkabko A, Rodriguez L, Magen C, Schaffer B (2012) Geometric phase analysis of the lattice distortion in $SrTiO_{3-x}$: Ny single crystal and defects produced by microwave NH_3 plasma. 15th European Microscopy Congress, EMC 2012. Available at www.emc2012.org.uk/documents/Abstracts/Abstracts/EMC2012_0912.pdf. Accessed September 25, 2015.
38. Imai T, Putaux J-L, Sugiyama J (2003) Geometric phase analysis of lattice images from algal cellulose microfibrils. *Polymer (Guildf)* 44(6):1871–1879.
39. Hÿtch M, Snoeck E, Kilaas R (1998) Quantitative measurement of displacement and strain fields from HREM micrographs. *Ultramicroscopy* 74(3):131–146.
40. Zhu Y, Ophus C, Ciston J, Wang H (2013) Interface lattice displacement measurement to 1pm by geometric phase analysis on aberration-corrected HAADF STEM images. *Acta Mater* 61(15):5646–5663.
41. Cawthorne C, Fulton EJ (1967) Voids in irradiated stainless steel. *Nature* 216(5115): 575–576.
42. Shewmon PG (1971) Radiation-induced swelling of stainless steel. *Science* 173(4001): 987–991.
43. Evans JH (1971) Observations of a regular void array in high purity molybdenum irradiated with 2 MeV nitrogen ions. *Nature* 229(5284):403–404.
44. Krishan K (1980) Kinetics of void-lattice formation in metals. *Nature* 287(5781): 420–421.
45. Evans JH (1979) Radiation-induced shrinkage of voids in molybdenum and TZM. *Nature* 278(5706):728–729.
46. Evans JH (1979) Mechanisms for radiation-induced shrinkage of voids - Reply. *Nature* 280(5719):253–254.
47. Krishan K, Nandedkar RV (1979) Mechanisms for radiation-induced shrinkage of voids. *Nature* 280(5719):253–253.
48. Evans J (1980) Void swelling and irradiation-induced void shrinkage in neutron irradiated molybdenum and TZM. *J Nucl Mater* 88(1):31–41.
49. Norris DI (1970) Voids in nickel irradiated with electrons after previous argon ion bombardment. *Nature* 227(5260):830–831.
50. Howitt DG, Mitchell TE (1981) Electron-irradiation damage in alpha-Al_2O_3. *Philos Mag A* 44(1):229–238.
51. Nelson DGA, McLean JD, Sanders JV (1982) High-resolution electron microscopy of electron irradiation damage in apatite. *Radiat Eff Lett* 68(2):51–56.
52. Wang LM, et al. (2000) Irradiation-induced nanostructures. *Mater Sci Eng A* 286(1): 72–80.
53. Mullins WW (1957) Theory of the thermal grooving. *J Appl Phys* 28(3):333–339.
54. Kuczynski GC (1949) Study of the sintering of glass. *J Appl Phys* 20(12):1160–1163.
55. Eggers J (1998) Coalescence of spheres by surface diffusion. *Phys Rev Lett* 80(12): 2634–2637.